Asociación Argentina de Mecánica Computacional

Mecánica Computacional Vol XXXI, págs. 631-649 (artículo completo)
Alberto Cardona, Paul H. Kohan, Ricardo D. Quinteros, Mario A. Storti (Eds.)
Salta, Argentina, 13-16 Noviembre 2012

SEISMIC REFLECTIVITY OF A CARBON DIOXIDE FLUX

Julián L. Gómez and Claudia L. Ravazzoli

CONICET and Departamento de Geofísica Aplicada, Facultad de Ciencias Astronómicas y Geofísicas, Universidad Nacional de La Plata, Paseo del Bosque s/n, La Plata, Argentina,
jgomez@fcaglp.unlp.edu.ar, http://www.fcaglp.unlp.edu.ar/~jgomez

Keywords: Two-phase flow, CO_2 sequestration, Relaxation method, Seismic reflectivity

Abstract. In the context of the geological storage of carbon dioxide (CO_2), the characterization of the injected CO_2 in a reservoir is of prime importance for volume capacity evaluation and long-term site performance. In this article, we aim to characterize a CO_2 accumulation in a deep layered aquifer by means of its seismic reflectivity. For modeling the vertical distribution of CO_2 saturation in the reservoir, we solve the Buckley-Leverett equation with discontinuous flux function, which describes two-phase flow in porous stratified media. To solve this equation numerically we employ a finite-difference relaxation scheme. The scheme entails an upwinding reconstruction for the spatial derivatives and an implicit-explicit Runge-Kutta scheme for time integrations. Once the vertical distribution of CO_2 is obtained, we use a matrix propagator algorithm to compute in the frequency domain, the generalized reflectivity of the reservoir due to the injected gas. The behavior of this reflectivity controls the amplitude of seismic wave reflections and strongly conditions the detectability of the CO_2 volume in the space-time domain. The numerical approach used in this article is easy to implement and allows to quantify the reflectivity of the carbon dioxide distribution in a practical way. We show that the frequency behavior of the reservoir reflectivity may help to interpret the vertical accumulation of CO_2, which can be useful as a basis for time-lapse geophysical monitoring.

1 INTRODUCTION

As a strategy to reduce and stabilize industrial carbon dioxide emissions in the atmosphere, CO_2 injection into geological repositories such as depleted hydrocarbon reservoirs and saline aquifers are taking place worldwide. To evaluate the storage performance of this repositories, it is mandatory to monitor the distribution of the injected carbon dioxide volumes. Seismic monitoring of these underground CO_2 accumulations is a topic of current interest in the branch of applied geophysics.

The CO_2 reservoir considered in this article is modeled after the Sleipner site at the North Sea. Sleipner is a large high-porosity sandy aquifer located at a depth from 700 to 1000 m that has been used as a CO_2 storage reservoir since 1996. The upward migration of the injected supercritical CO_2 due to buoyancy effects amounts to about 250 m and seems to have been stopped by the caprock situated at the top of the formation (Chadwick et al., 2005). The presence of a layered system of low permeability barriers in the reservoir have been revealed by time-lapse seismic surveys. Seismic velocities and densities for the Utsira sandstone and the shale barriers are shown in Table 1.

Lithology	V_p [m/s]	V_s [m/s]	ρ [kg/m^3]
Sandstone	2050	640	2050
Shale	2270	850	2100

Table 1: Seismic velocities and density of the Sleipner sandstone and shale at the 100% brine saturated pre-injection state, taken from Chadwick et al. (2005).

In this work we will analyze the generalized seismic reflectivity of compressional waves due to the inflow of a vertical distribution of CO_2 within the aquifer. We will show that capillarity effects can be disregarded and that strong evidence on the character of the CO_2 plume can be derived from the inspection of the time-frequency behavior of the seismic reflectivity. The simulation of the carbon dioxide flow in the Sleipner aquifer is achieved with a finite-difference relaxation method. A propagator method then allows us to obtain the reflectivity in the frequency domain generated by the carbon dioxide flux.

This article is organized as follows. The theory of the two-phase flow in porous media is provided in Section 2. Its numerical implementation is then described in Section 3. Next, in Sections 4 and 5 we introduce the matrix propagator method for the reflectivity calculation and the time-frequency decomposition of seismograms. In Section 6 we present the procedure for the characterization of the CO_2 distribution. In particular, in Section 6.1 we analyze the effects of capillary pressure in the saturation front. In Sections 6.2 and 6.3 we examine the reflectivity and seismic impact of a CO_2 vertical distribution on two reservoir scenarios. Finally, we end up with the conclusions in Section 7.

2 GOVERNING EQUATIONS

The system that describes the physics of a two-phase immiscible flow in a porous medium is given by a mass conservation law, Darcy's constitutive relation and necessary state equations

for fluid saturation and capillary pressure. These are

$$\begin{aligned} \frac{\partial(\phi\rho_l S_l)}{\partial t} + \boldsymbol{\nabla}\cdot(\rho_l \boldsymbol{v}_l) = 0, \quad l = w, g; \\ \boldsymbol{v}_l = -\frac{k_{rl}(S_l)}{\mu_l}\boldsymbol{K}\boldsymbol{\nabla}(p_l + \rho_l g z), \quad l = w, g; \\ p_g - p_w = p_c(S_g); \\ S_w + S_g = 1. \end{aligned} \tag{1}$$

where ϕ is the porosity of the medium, ρ_l, S_l and $\boldsymbol{v}_l$ are the density, saturation and flow velocity vector of phase l respectively. $\boldsymbol{K}$ is the absolute permeability tensor, k_{rl}, p_l and μ_l are the relative permeability, pressure and viscosity of phase l. g is the gravity field modulus and p_c the capillary pressure. Index $l = w$ refers to the brine phase and $l = g$ to the carbon dioxide phase.

For a rigid isotropic medium, porosity, absolute and relative permeabilities are assumed to be independent of time and the permeability tensor $\boldsymbol{K}$ becomes a scalar K. In addition, assuming that the hydraulic parameters of the medium vary only on the vertical direction z and if the fluids are assumed to be incompressible, then the conservation of mass and Darcy's law can be written in the form

$$\phi(z)\frac{\partial S_l}{\partial t} + \boldsymbol{\nabla}\cdot(\boldsymbol{v}_l) = 0, \quad l = w, g; \tag{2}$$

$$\boldsymbol{v}_l = -\frac{k_{rl}}{\mu_l}K(z)(\boldsymbol{\nabla}p_l + \rho_l g \boldsymbol{e}_z), \quad l = w, g, \tag{3}$$

where $\boldsymbol{e}_z$ denotes the unit vector along the z axis. Following Mouche et al. (2010), we introduce the total flow velocity vector as

$$\boldsymbol{v}_g + \boldsymbol{v}_w = \boldsymbol{v}, \tag{4}$$

then, by using Darcy's law we can express the velocity of the gaseous phase as follows

$$\boldsymbol{v}_g = \frac{k_{rg}}{k_{rg} + Mk_{rw}}\boldsymbol{v} + \frac{k_{rg}k_{rw}/\mu_w}{k_{rg} + Mk_{rw}}K(\rho_w - \rho_g)g\boldsymbol{\nabla}z - \frac{k_{rg}k_{rw}/\mu_w}{k_{rg} + Mk_{rw}}K\boldsymbol{\nabla}p_c, \tag{5}$$

where $M = \frac{\mu_g}{\mu_w}$ is the viscosity ratio. This expression entails the three forces that drive the CO_2 vertical migration: injection, gravitation and capillarity (Hayek et al., 2009).

In terms of the fractional flux function,

$$f(S_g) = \frac{k_{rg}(S_g)}{k_{rg}(S_g) + Mk_{rw}(S_g)}, \tag{6}$$

the 1D saturation equation for the vertical distribution of CO_2 in the porous medium is given by

$$\phi(z)\frac{\partial S_g}{\partial t} + \frac{\partial}{\partial z}\left[f(S_g)\left(v + \frac{k_{rw}(S_g)}{\mu_w}K(z)(\rho_w - \rho_g)g - \frac{k_{rw}(S_g)}{\mu_w}K(z)\frac{\partial p_c}{\partial z}\right)\right] = 0. \tag{7}$$

If we choose to describe the migration as a buoyancy driven process, then $\boldsymbol{v} = \boldsymbol{0}$ (Hayek et al., 2009). This means that at each point of the medium, the sum of the fluid and gaseous phase velocities are zero. The brine phase flows downward while the CO_2 flows upward, with velocities equal in magnitude (Cunha et al., 2004). Then the saturation equation can be written as

$$\phi(z)\frac{\partial S_g}{\partial t} + \frac{\partial}{\partial z}F(S_g, z) = 0, \tag{8}$$

being $F(\cdot)$ the global flux function (Mouche et al., 2010),

$$F(S_g, z) = \frac{1}{\mu_w} f(S_g) k_{rw}(S_g) K(z) \left((\rho_w - \rho_g) g - \frac{\partial p_c}{\partial z} \right). \tag{9}$$

To solve this balance equation for the CO_2 phase, an expression for the relative permeabilities and the capillary pressure are needed. We will use the well-known Brooks-Corey expressions (Brooks and Corey, 1966) for relative permeabilities,

$$\begin{aligned} k_{rw}(S_g) &= (1 - S_{eg})^{\frac{2+3\lambda}{\lambda}} \\ k_{rg}(S_g) &= S_{eg}^2 \left[1 - (1 - S_{eg})^{\frac{2+\lambda}{\lambda}} \right] \end{aligned} \tag{10}$$

where λ is the pore size distribution index and

$$S_{eg} = \frac{S_g - S_{rg}}{1 - S_{rg} - S_{rw}} \tag{11}$$

is the effective gas saturation. S_{rw}, S_{rg} denote the residual brine and CO_2 saturations which satisfy $S_{rw} + S_{rg} < 1$. The capillary pressure is modeled combining the Leverett function (Leverett, 1941) and Brooks and Corey (1966) law in the following form

$$p_c(S_g, z) = \sigma \sqrt{\frac{\phi}{K(z)}} (1 - S_{eg})^{-1/\lambda}, \tag{12}$$

where σ is the interfacial tension between brine and CO_2.

A measure of the relative importance of capillary effects to buoyancy is given by the capillarity number given by

$$N_c = \frac{\sigma \sqrt{\frac{\phi}{K_0}}}{(\rho_w - \rho_g) g H}, \tag{13}$$

where H is a characteristic length, which in this article is taken as the length of the reservoir and K_0 is a characteristic permeability of the medium. As it can be seen, N_c is expected to be small at the reservoir scale, where $H >> 1$. In what follows we will drop the subindex g to denote the CO_2 saturation, $S \equiv S_g$, and assume constant porosity in the reservoir, $\phi(z) = \phi$ in agreement with Hayek et al. (2009); Mouche et al. (2010).

3 NUMERICAL APPROACH

Many finite-difference approaches exist in the literature on the study of conservation laws such as Equation (8). For the case of the saturation equation, due to the shock-rarefaction nature of its solutions, different schemes have been proposed and tested, such as Godunov's methods (Kaasschieter, 1999), flux limiters (Sweby, 1984), composite schemes (Dubey, 2010), domain decomposition (Herty et al., 2007), relaxation methods (Seaïd, 2006) and implicit pressure explicit saturation schemes (Negara et al., 2011).

Since the Sleipner field contains thin intra-bed shale layers acting as temporal permeability barriers to the CO_2 flow, we chose from the available literature about finite difference methods, one which can efficiently handle discontinuities in the global flux function. Then, following the method presented by Seaïd (2006), we will use a relaxation approximation, which turns the nonlinear equation to a semilinear diagonalizable problem. The main advantage of this

approach is the simplicity of the resulting scheme that accurately solves the conservation law in the presence of permeability discontinuities.

The numerical simulation of the vertical migration of CO_2 in a reservoir of length H, can be resumed by the following system

$$\begin{aligned} \frac{\partial S(z,t)}{\partial t} + \frac{\partial}{\partial z} F(S, K(z)) = 0, \quad z \in [0, H], \quad t > 0, \\ S(z, t=0) = S_0(z), \quad z \in [0, H]; \qquad (14) \\ S(z=0, t) = S_b, \quad \forall t, \\ F(S, K(z)) = 0, \quad \text{for} \quad z = H. \qquad (15) \end{aligned}$$

where $S_0(z)$ is the initial saturation profile and S_b is a boundary condition at the base of the reservoir, that simulates a constant flow of carbon dioxide entering the reservoir from a distant injection point. The zero flux condition at the top of the reservoir means that the CO_2 will not leak into the caprock, which is assumed to be a perfect seal in this work.

According to the previous description, the reservoir is modeled as an assemblage of two lithologies, the highly permeable part associated to the unconsolidated Utsira sandstone and the low-permeable shale layers. Consequently, the permeability function is given by

$$K(z) = \begin{cases} K_1 & \text{if } z \in \text{sandstone interval}, \\ K_2 < K_1 & \text{if } z \in \text{shale interval}. \end{cases} \qquad (16)$$

The relaxation system associated to Equation (15) is (Seaïd, 2006; Jin and Z., 1995)

$$\begin{aligned} \frac{\partial S}{\partial t} + \frac{\partial v}{\partial z} = 0, \\ \frac{\partial v}{\partial t} + \Lambda^2 \frac{\partial S}{\partial z} = -\frac{1}{\epsilon} \left(v - F(S(z), K(z)) \right); \qquad (17) \\ S(z, t=0) = S_0(z), \quad v(z, t=0) = F(S_0(z), K(z)), \qquad (18) \end{aligned}$$

where $v \in \mathbb{R}$ is the relaxation variable, $\epsilon \in [0, 1]$ is the relaxation rate and Λ is the characteristic speed. As $\epsilon \to 0^+$ the solution of the relaxation system is expected to converge to the solution of the conservation law.

The discrete counterpart of the relaxation system reads

$$\begin{aligned} \frac{\mathrm{d}S_i}{\mathrm{d}t} + \frac{v_{i+1/2} - v_{i-1/2}}{\Delta z} = 0, \\ \frac{\mathrm{d}v_i}{\mathrm{d}t} + \Lambda^2 \frac{S_{i+1/2} - S_{i-1/2}}{\Delta z} = -\frac{1}{\epsilon} \left(v_i - F(S_i, K_i) \right). \qquad (19) \end{aligned}$$

The time integration of the relaxation stage in Equation (19) is performed using a second-order implicit-explicit Runge-Kutta algorithm. The calculation of the numerical fluxes $S_{i\pm1/2}$ and $u_{i\pm1/2}$ are given by a upwind MUSCL scheme. We refer to Seaïd (2006) for further details.

As the algorithm is uniformly stable, the time step is adjusted as

$$\Delta t = \text{CFL} \frac{\Delta z}{\Lambda^2}, \qquad (20)$$

provided that CFL $\leqslant 1$. The characteristic speeds Λ are obtained at each time step as

$$\Lambda = \max_z \left\{ \frac{\partial}{\partial z} F(S, K(z)) \right\} + \tau, \qquad (21)$$

where τ is a safety parameter that avoids Λ to become close to zero (Seaïd, 2006; Herty et al., 2007).

The numerical code written for this article has been validated trough the matching of the results from the works of Hayek et al. (2009) and Seaïd (2006). The parameters used for the reservoir flow simulation and those of the relaxation scheme are given in Tables 2 and 3 respectively.

Property	Value	Units
Porosity of sand, ϕ	0.37	[]
Permeability of sand, K_1	1×10^{-12}	[m^2]
Permeability of shale, K_2	5×10^{-14}	[m^2]
Density of brine, ρ_w	1040.0	[kg/m^3]
Density of CO_2, ρ_g	700.0	[kg/m^3]
Viscosity of brine, η_w	0.25×10^{-3}	[kg/m s]
Viscosity of CO_2, η_g	4.38×10^{-5}	[kg/m s]
Residual saturation of brine, S_{rw}	0.20	[]
Residual saturation of CO_2, S_{rg}	0.05	[]
Entry Pressure, P_0	1.43×10^3	[Pa]
Pore size distribution, λ	2	[]

Table 2: Main parameters for the reservoir. Data has been collected from Audigane et al. (2007); Chadwick et al. (2004); Hayek et al. (2009) and Mouche et al. (2010).

Property	Value	Units
Grid resolution, Δx	0.126	[m]
CFL number	0.5	[]
Relaxation rate, ϵ	1×10^{-10}	[]
Safety parameter, τ	1×10^{-6}	[m/s]

Table 3: Relaxation scheme parameters.

4 THE SEISMIC REFLECTIVITY

Once the vertical distribution of the carbon dioxide flux has been simulated, the reservoir reflectivity response at normal incidence is obtained using a matrix propagator method for layered elastic media. This approach is based on the continuity of particle displacements and stress components at the interfaces between sets of plane layers embedded between two half-spaces. The resulting equations can be written as a recursive algorithm that allows the computation of the generalized complex reflection and transmission coefficients of the multilayer model (Tsvankin, 1995; Brekhovskik, 1980). From the physical and geometrical parameters of each layer, the propagator matrix $\mathcal{P}$ is computed by the product

$$\mathcal{P} = \prod_{k=1}^{n} \mathcal{M}_k \left(V_p^k,\, V_s^k,\, \rho_b^k,\, h^k;\, f \right), \tag{22}$$

where $\mathcal{M}_k$ is a 4×4 matrix that depends on seismic velocities, V_p^k, V_s^k, bulk density, ρ_b^k, and thickness h^k of layer k, being n the number of layers in the model. It is also a function of

the incident plane wave frequency, f. Knowing the reservoir propagator matrix, $\mathcal{P}$, from equation (22) and given the displacement-stress vector, $\boldsymbol{\mathcal{A}}^T = [u_x, u_z, \tau_{zz}, \tau_{zx}]$ (where T denotes the transpose), at the half-spaces, from the continuity of the displacements u_x, u_z and stresses τ_{zz}, τ_{zx} across the model, we have

$$\boldsymbol{\mathcal{A}}_{n+1} = \mathcal{P}\, \boldsymbol{\mathcal{A}}_0. \tag{23}$$

$\boldsymbol{\mathcal{A}}_0$ and $\boldsymbol{\mathcal{A}}_{n+1}$ are the corresponding displacement-stress vectors at the top and bottom half-spaces respectively. From equation (23) we can obtain the generalized complex potential reflection coefficients for P waves, denoted as $R_{pp}\,(f)$. To solve this system directly in terms of the potential amplitudes, we first write the displacement-stress vectors as functions of the displacement Helmholtz's potentials, $\boldsymbol{u} = \boldsymbol{\nabla}\Phi + \boldsymbol{\nabla} \times \boldsymbol{\psi}$, where Φ is the potential associated to P waves and $\boldsymbol{\psi}$, the potential associated to SV waves. For a plane wave, these potentials have an expression which is linear in their amplitudes, e.g. $\Phi = A \exp i\,(k_x x - k_z z - \omega t) + B \exp i\,(k_x x + k_z z - \omega t)$ for the P-wave in the first halfspace; where A and B are the amplitudes of the incident and reflected waves respectively, i is the imaginary unit and $\omega = 2\pi f$, being f the frequency of the incident plane wave. Once the system is solved, we can obtain the normal-incidence P-wave reflection coefficient from the related potential amplitudes, in this case $R_{pp}\,(f) = B/A$.

To compute the lithological properties, given the CO_2 bulk modulus $\mathcal{K}_g$ and density ρ_g, we can estimate the effective bulk density, ρ_b, and bulk modulus, $\mathcal{K}$, of each layer composing the model reservoir as a function of its carbon dioxide saturation and spatial fluid distribution type - uniform $\mathcal{K}^G$, or patchy $\mathcal{K}^{\text{pat}}$. The bulk density, ρ_b, of the saturated layer is calculated as

$$\rho_b = (1-\phi)\,\rho_m + \phi\,(S_w \rho_w + S_g \rho_g)\,, \tag{24}$$

where ρ_m is the mineral grain density and ρ_w and ρ_g, are brine and CO_2 density respectively. Under the assumption of elasticity and isotropy seismic velocities of compressional V_p and shear waves V_s are given by

$$V_p{}^2 = \frac{\mathcal{K} + \frac{4}{3}\mu}{\rho_b} \quad \text{and} \quad V_s{}^2 = \frac{\mu}{\rho_b}, \tag{25}$$

being $\mathcal{K}$ the bulk modulus of the fluid saturated rock and μ the shear modulus of the rock's dry matrix.

Assuming no dissipative effects or chemical interactions within the frame and fluids, if we consider the CO_2 and brine as mixed uniformly at very small scales, we can estimate the rock's bulk modulus $\mathcal{K}$ through Gassmann's relation, which can be written as (Mavko et al., 2011; Smith et al., 2003),

$$\mathcal{K}^G(S_g) = \mathcal{K}_m \left(\frac{\mathcal{K}_d + Q}{\mathcal{K}_m + Q} \right), \quad \text{with} \quad Q = \frac{\mathcal{K}_f(S_g)\,(\mathcal{K}_m - \mathcal{K}_d)}{\phi\,(\mathcal{K}_m - \mathcal{K}_f(S_g))}, \tag{26}$$

where $\mathcal{K}_d$ and $\mathcal{K}_m$ are the bulk modulus of the dry matrix and the mineral grains respectively; $\mathcal{K}_f$ is the effective fluid compressibility calculated by the isostress Reuss average of individual fluid bulk moduli:

$$\frac{1}{\mathcal{K}_f(S_g)} = \frac{S_w}{\mathcal{K}_w} + \frac{S_g}{\mathcal{K}_g}. \tag{27}$$

If we consider patches of CO_2 and brine, then, for seismic frequencies and arbitrary patch geometry, the rock bulk modulus is better described as (Mavko et al., 2011; Mavko and Mukerji,

1998),

$$\frac{1}{\mathcal{K}^{\text{pat}}(S_g)+\frac{4}{3}\mu}=\frac{S_w}{\mathcal{K}^G_{S_w=1}+\frac{4}{3}\mu}+\frac{S_g}{\mathcal{K}^G_{S_g=1}+\frac{4}{3}\mu} \tag{28}$$

where $\mathcal{K}^G_{S_w=1}$ and $\mathcal{K}^G_{S_g=1}$ are the Gassmann's modulus for the rock fully saturated with brine and CO_2 respectively. This completes the set of physical parameters needed by the propagator matrix algorithm for each layer of the reservoir. As a final stage, a velocity average between the homogeneous and patchy cases is used to account for the lack of knowledge about the in-situ CO_2-brine distribution,

$$V_p=\tfrac{1}{2}\left(V_p|_{\mathcal{K}=\mathcal{K}^G}+V_p|_{\mathcal{K}=\mathcal{K}^{\text{pat}}}\right). \tag{29}$$

The rock physics parameters used for the reservoir are shown in Table 4. The shale bulk modulus for mineral grains was derived from the Nørdland shale mineralogical composition considered in Audigane et al. (2007), where chalcedony was changed to quartz and the chlorite bulk modulus was taken from Katahara (1996); the rest of the mineral bulk moduli are from Mavko et al. (2011). Shale porosity was taken from Carcione et al. (2006). The other entries in the table were taken from Chadwick et al. (2005). The model parameters are within the range of possibilities in the reservoir.

Property	Value	Units
Utsira bulk modulus of mineral grains, K_0^{Utsira}	36.9	[GPa]
Shale bulk modulus of mineral grains, K_0^{shale}	22.72	[GPa]
Porosity of shale rock, ϕ^{shale}	0.25	[]
Brine bulk modulus, K_w	2.305	[GPa]
CO_2 bulk modulus, K_g	0.08	[GPa]

Table 4: Relevant rock properties for fluid substitution.

5 SYNTHETIC SEISMOGRAMS AND TIME-FREQUENCY DECOMPOSITION

Time-domain synthetic seismograms are obtained by an inverse Fourier transform of the product of the reflectivity $R_{pp}(f)$ and a seismic source wavelet spectrum $A(f)$. In this article we consider a Ricker wavelet, of spectrum (Zhang and Ulrych, 2002)

$$A(f)=\frac{2}{\sqrt{\pi}}\left(\frac{f}{f_m}\right)^2\exp\left(-\frac{f^2}{f_m^2}\right), \tag{30}$$

where f_m is the dominant frequency.

As it is well known, when the wavelengths of seismic waves are greater or on the order of layer thicknesses, interference effects can take place. This gives rise to strong frequency dependence in the reflectivity of the medium, a phenomenon called *reflectivity dispersion* (Liner and Bodmann, 2010). Some examples can be found in the work recently published by Gomez and Ravazzoli (2012), where a parametric analysis of reflection amplitudes versus frequency associated to linear CO_2 saturation-depth profiles was presented. In connection with this subject, the development of spectral decomposition methods and time-frequency representations are useful tools that allow for the investigation of the frequency dependent behavior on seismic reflection data. A time-frequency representation of a seismic signal can enhance information which otherwise could be difficult to visualize in the time domain. As opposed to standard Fourier transforms, the frequency decomposition can show the variation through seismic travel time of

the spectral content of a signal (Chakraborty and Okaya, 1995). Any algorithm that produces a continuous time-frequency mapping of a seismic trace is known as *spectral decomposition*. As pointed out by Castagna and Sun (2006), the spectral decomposition of a signal is non unique.

One of the possible approaches is to use the *short time Fourier transform* (STFT), which for a given signal can be calculated by using a moving window on the time domain signal and computing its Fourier spectra at each window step. This way, a mapping of a time domain signal into a joint time-frequency domain (spectrogram) is achieved. The STFT at time τ and frequency f is defined as (Chakraborty and Okaya, 1995)

$$STFT\,(\tau, f) = \int s(t) w(t-\tau) e^{-i2\pi f t} \mathrm{d}t, \tag{31}$$

where $s(t)$ is the time-domain seismic trace and $w(t)$ a $\mathbb{R} \rightarrow \mathbb{R}$ window function. The time-frequency resolution of this transformation is completely determined by the choice of the window function (Chakraborty and Okaya, 1995; Castagna and Sun, 2006). Although the STFT is known for its relatively poor time resolution and spectral distortion due to windowing (Chakraborty and Okaya, 1995), since the reflectivity function that generates the synthetic seismogram is completely known, an accurate spectra versus time representation can be calculated from the response of the convolution of the reflectivity with a time-domain unit spike (Liner and Bodmann, 2010). From this time-frequency representation the essential features which are important for interpretation can be captured, much in the way as the criteria proposed by Castagna and Siegfried (2003), where distinct seismic arrivals should appear as distinct events on the time-frequency space, side lobes on the seismogram do not appear as isolated frequency-time events and the time span of an event are similar on both the time-frequency domain and the seismic trace.

Another useful seismic attribute is the so-called *waveform simulation*, introduced by Liner and Bodmann (2010). It is used as a detection tool, that from a properly windowed seismic trace $s(t)$, in our case presumed of being from a CO_2 accumulation, generates a time-frequency version $g(t, f)$ given by

$$g(t, f) = \mathrm{Re}\left[S(f)\, e^{-i\,2\pi f t}\right], \tag{32}$$

where $S(f) \leftrightarrow s(t)$ is the Fourier transform of the seismic trace, i the imaginary unit and Re denotes the real part. The seismic traces now spread in the time-frequency plane can be inspected for amplitude patterns due to the presence of CO_2.

6 CHARACTERIZING THE CO_2 SATURATION DISTRIBUTION

The coupled numerical modeling of the carbon dioxide flux and the calculation of its seismic reflectivity and spectral responses aims at monitoring the effects of the vertical geological storage of CO_2. Although the migration of carbon dioxide in real media is a complex process, as pointed out by Mouche et al. (2010), a one-dimensional approach for the Sleipner site may be useful for feasibility assessments and as a basis for generalizations to more complex and higher dimensional models.

6.1 Capillary effects

Capillary forces tend to prevent the formation of sharp saturation discontinuities (Buckley and Leverett, 1942; Goumiri et al., 2011), for this reason the vertical distribution of CO_2 will be a smoother version of the one obtained when neglecting capillarity in the numerical implementation of the saturation Equation (8). In this section we investigate whether it is reasonable to

disregard the effects due to capillarity in our reservoir simulation. As pointed out by Goumiri et al. (2011), the most notable effect of capillary pressure is that it increases the spread of the saturation front of the advancing fluid, in this case carbon dioxide. This could lead to an erroneous position of the CO_2/brine contact in case capillarity effects are important.

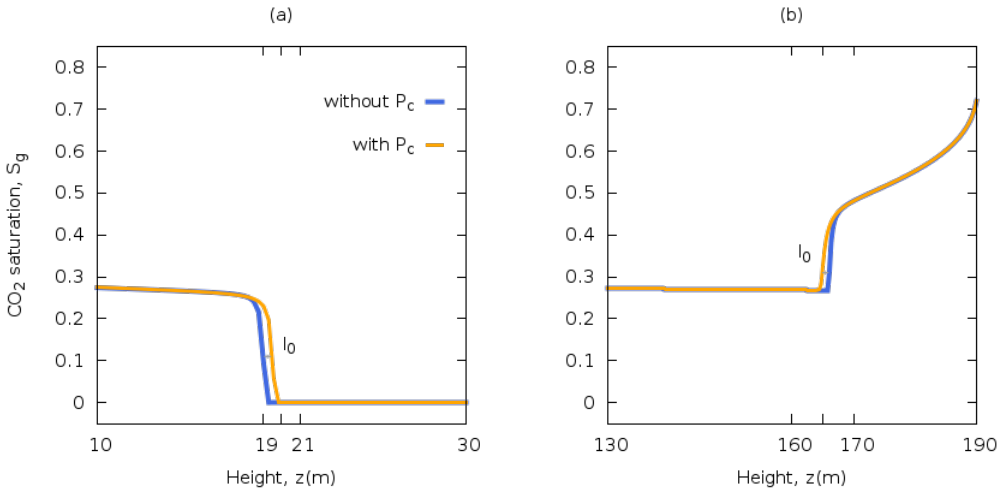

Figure 1: CO_2 saturation profile with and without capillary pressure. *(a)* near reservoir bottom: $l_0 \approx 0.5$ m, time is $t = 13$ days. *(b)* below the caprock: $l_0 \approx 1.3$ m, time is $t = 150$ days. Entry pressure $P_0 = 1.43$KPa.

An estimation of the front variation due to capillarity is shown in Figure 1 when the plume starts to spread *(a)* and when CO_2 has started to accumulate below the caprock *(b)*. For simplicity, we have not included the presence of the intra reservoir shale barriers in this analysis. The entry pressure was taken to be $P_0 = 1.43$ KPa (Audigane et al., 2007). As can be seen, the CO_2 front variation l_0 is on the order of meters in our reservoir simulation. As noticed by (Goumiri et al., 2011), capillary effects on the total vertical spread of the CO_2 plume are also negligible. We have tested as well an entry pressure of 4.0 KPa as reported by Chadwick et al. (2009), being l_0 on the order of 1 m when the plume leaves the injection point and on the order of 5 m when starts to accumulate. From these results we think reasonable to disregard the increase on the penetration of the saturation front due to capillarity in the context of this work, since the resulting vertical gas distribution will be only slightly different when considering this effect (Negara et al., 2011). By neglecting capillarity, the numerical implementation becomes simpler and faster, since capillary pressure effects requires a space discretization capable of sampling the centimeter scale; which can render typical large scale computational reservoir models unnecessarily expensive.

6.2 Monitoring the CO_2/brine contact for a simple case

We begin the CO_2 flow/reflectivity analysis with a simple geological scenario. The reservoir consists of a halfspace of shale caprock, a 100 m layer of brine saturated Utsira sandstone with absolute permeability K_1, a 5 m shale barrier of absolute permeability K_2 and another halfspace of sandstone. We consider the CO_2 injection point placed at 100 m below the shale barrier.

The purpose of this geometry is to test the detectability and frequency patterns associated with the vertical distribution of carbon dioxide. The thickness of the sandstone layer will make the geological contacts seismically resolvable for an assumed 30 Hz Ricker wavelet. Careful selection of STFT parameters needed to create meaningful spectra lead in this case to consider a

Hamming time window of 22 ms and a window increment of one sample that lead to a complete coverage of the time domain. The focus in this examples is on the study of the time position of the fluid/fluid contacts rather than their detailed frequency content.

Figure 2 clearly shows the seismic events due to the geological contacts at the pre-injection state. The reflection signal coming from the thin shale is composed of the interference of two wavelets as is seen in the time-frequency domain.

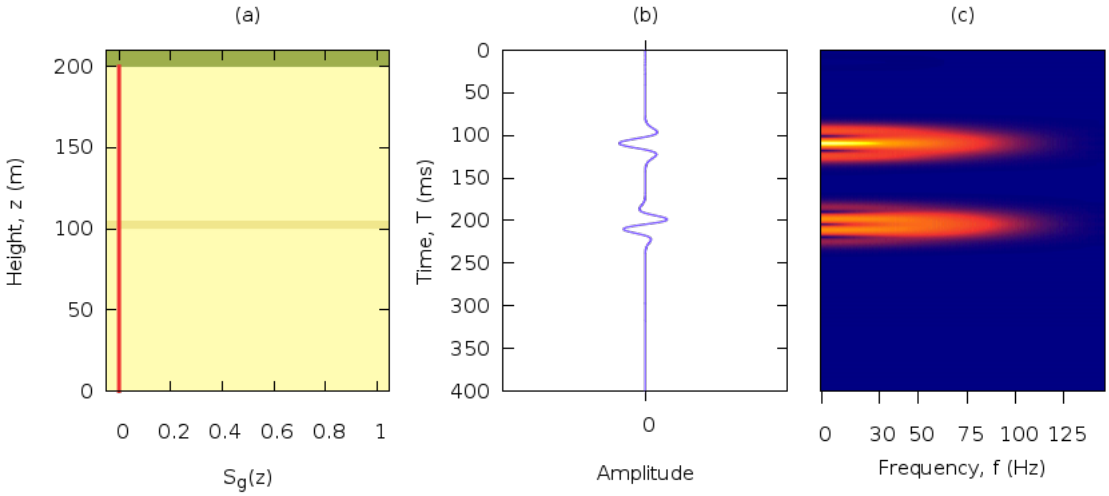

Figure 2: *(a)* Vertical CO_2 distribution , *(b)* synthetic trace and *(c)* STFT spectrogram for a thick layer reservoir at the pre-injection state.

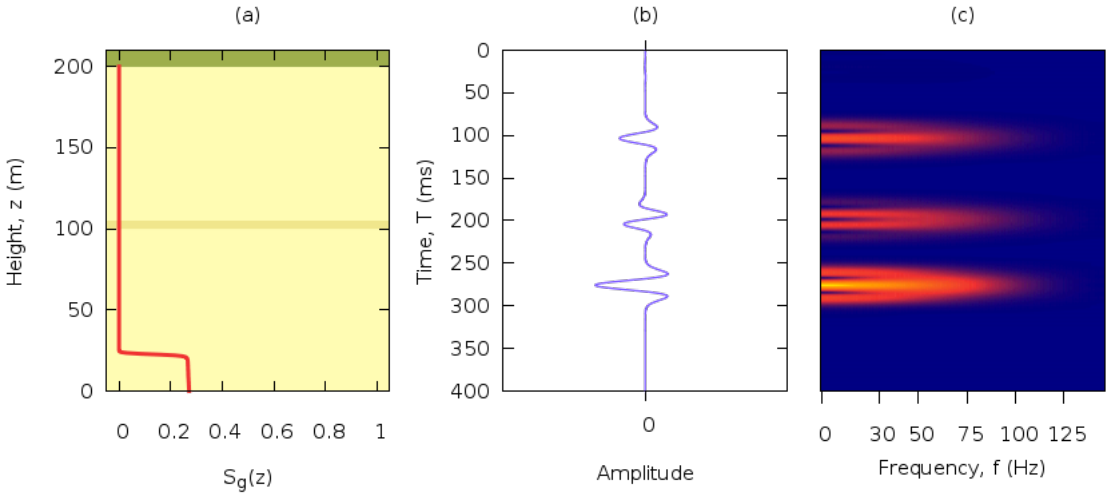

Figure 3: *(a)* Vertical CO_2 distribution , *(b)* synthetic trace and *(c)* STFT spectrogram for a thick layer reservoir when CO_2 begins to displace the in situ brine in its way to the shale barrier.

Figure 3 (a)-(c) show the CO_2 saturation front entering the target reservoir, the CO_2/brine contact is readily visible in the synthetic traces and as a high energy event in the spectrogram. The contact has a higher impedance contrast than the caprock/sandstone layer, since the drop in

velocity in the sandstone due to the carbon dioxide generates a larger impedance contrast than the geological contacts of the reservoir.

When the CO_2 front reaches the shale barrier, the spectrogram still shows that the interference is resolvable even a time after it has already merged as one composite reflection in the synthetic trace. Once the carbon dioxide enters the barrier, two CO_2/brine contacts emerge: one going upwards and one, related to the CO_2 accumulation below the barrier (Figure 4), going downwards. Both events are clearly seen in both time and spectrogram. We also note that the shale barrier has gained a stronger energy response due to the presence of carbon dioxide. The upward fluid contact migrates and finally reaches the caprock. Its effect is to enhance the energy response of the geological contact and the generation of another fluid/fluid contact, related to the transition layer below the caprock (Figure 5). As we can see, this seismic contact has an opposite polarity to the previously upward contact, since now it is associated to the contrast between a lower CO_2 rich medium to a higher brine rich sandstone.

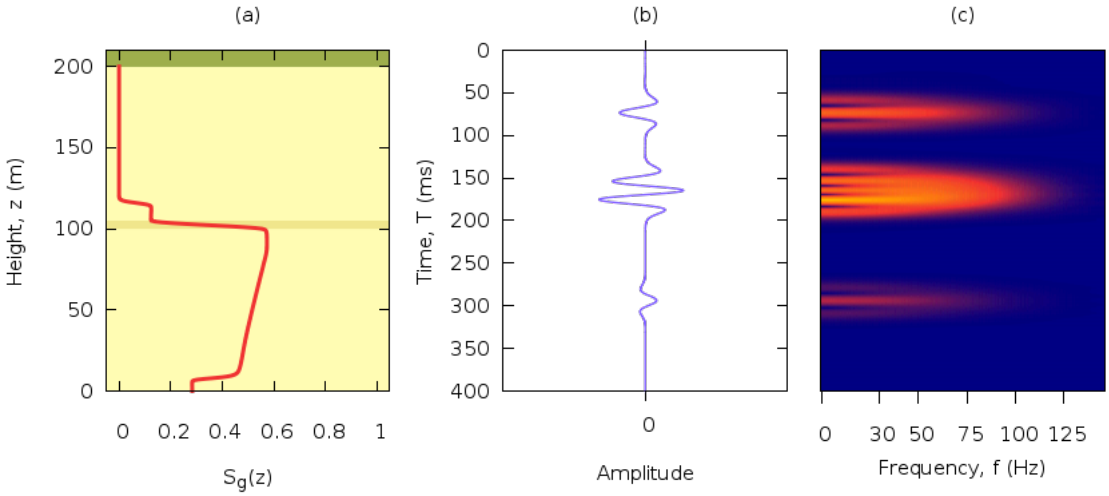

Figure 4: *(a)* Vertical CO_2 distribution , *(b)* synthetic trace and *(c)* STFT spectrogram for a thick layer reservoir when CO_2 has encountered the barrier and began its path to the caprock.

The overall effect of carbon dioxide injection is to enhance the seismic events related to the geological contacts, as is seen in the time-lapse data from the real Sleipner site (Chadwick et al., 2005). When the seismic signal fails to isolate the reflectors since there are too close in time, a closer monitoring of the CO_2 accumulation can be performed by following the migration of the fluid/fluid contacts in the time-frequency domain.

We will perform in the next section a similar analysis but on a reservoir that resembles more approximately the situation at Sleipner. This time, the mapping of the fluid/fluid contacts will not be possible.

6.3 Modeling the topmost CO_2 accumulation including intrabed shales

Here we analyze a reservoir model much closer to the geology of the Sleipner field, as shown in Figure 6. The reservoir entails 190 m and consists in a series of four shale layers with thickness equal to 5 m, embedded within the Utsira sandstone of absolute permeability K_1, according to the description given in Section 3. The thin shale barriers are separated by 30

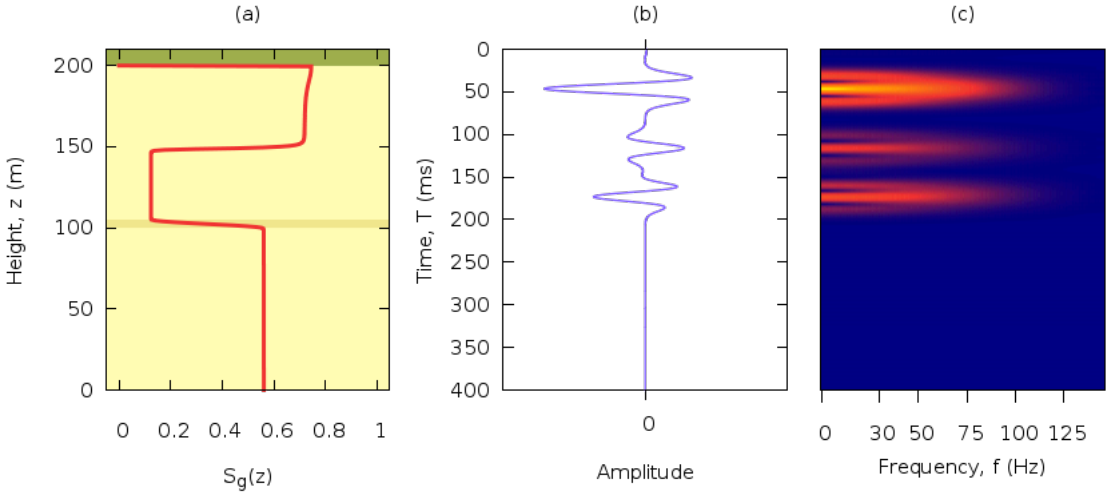

Figure 5: *(a)* Vertical CO_2 distribution , *(b)* synthetic trace and *(c)* STFT spectrogram for a thick layer reservoir when the CO_2 has started to accumulate below the caprock.

meters and are characterized by an absolute permeability K_2. The caprock is made of the same shale as the barriers. Injection of carbon dioxide takes place at the bottom of the column.

We will focus our analysis on the topmost accumulation of CO_2, between $160 < z < 190$ m, since its reflectivity and seismic response are expected to produce a strong seismic reflection. Figure 7 shows the topmost carbon dioxide distribution at several times.

The pre-injection $|R_{\text{PP}}(f)|$ for the topmost part of the reservoir is the expected AVF for a layer between two halfspaces as we can see in Figure 8(a). The sinusoidal character is directly related to the thickness of the layer (25 m) and inversely related to its P-wave velocity, which in this case is of the fully brine-saturated Utsira sandstone. When no CO_2 transition is present, we expect a sinusoidal character on the AVF completely defined by the layer thickness and its seismic velocity. The value of $|R_{\text{PP}}(f)|$ at $f = 0$ Hz is related to the impedance contrast between the caprock and the base of the topmost shale barrier.

The reflectivity character of the transition layer is readily evident in the AVF plots shown in Figure 8(b) and 8(c). The transition is characterized as a rupture of pre-injection sinusoidal character of $|R_{\text{PP}}(f)|$ related to a constant V_{P} layer. As the transition builds up, the AVF curve losses its asymmetry and eventually, when the CO_2 has reach a rather constant distribution with height after accumulating below the caprock, turns again into a sinusoidal character. By tracking the position and amplitude of the reflectivity lobes as the transition develops, some inference about its thickness could be achieved. In all the stages of the transition we observe that the peaks of the reflectivity lobes are not equal, so a distinctive feature of a transition is a selective AVF lobe attenuation.

Once the transition becomes a constant CO_2 saturation layer, the number of lobes in the reflectivity are different as we can see in Figure 8 *(d)* since this time the sandstone is almost fully saturated with carbon dioxide, having a lower V_{P} with respect to the pre-injection case. An estimation of the bulk CO_2 saturation, or residual brine saturation, in the layer at the post-injection state can be then obtained by searching for a velocity that matches the observed post-injection behavior through a fluid substitution procedure; where carbon dioxide saturation is increased up to a point where the post-injection sinusoidal character is obtained. We note also that the value of $|R_{\text{PP}}(f)|$ at $f = 0$ Hz is not zero anymore as in the pre-injection case due to

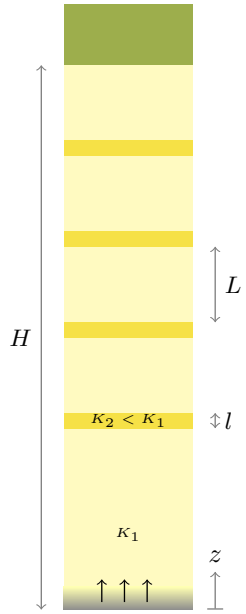

Figure 6: Sketch of the reservoir. The system is modeled as an alternation of highly permeable sandstone layers, separated by semi-permeable shale barriers. Dimensions are $H = 190\,\text{m}$, $L = 25\,\text{m}$ and $l = 5\,\text{m}$

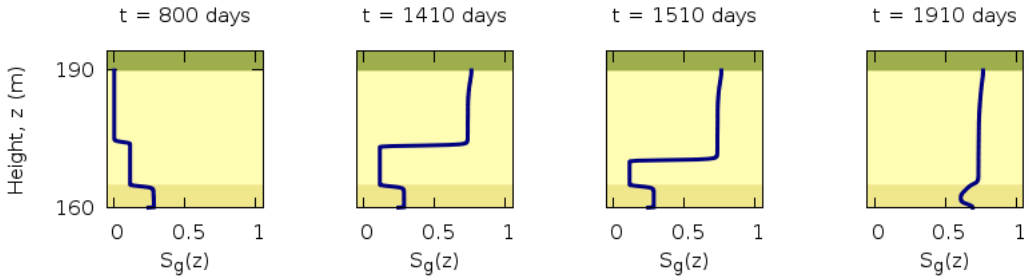

Figure 7: Vertical profiles of CO_2 in the reservoir top at several times; when no transition is present (t=800 days), when transition is developed (t=1410 and 1510 days) and transition becomes a constant CO_2 saturation layer (t=1910). Saturations in the range 160 to 190 m are 1% (t=800 days), 48% (t=1410 days), 55% (t=1510 days) and 72% (t=1900 days).

the presence of carbon dioxide in the permeable shale barrier.

6.4 Effect on wavelet amplitude spectrum

So far we have studied the reflection characteristics associated to plane monochromatic waves. In this section we analyze the effects of the vertical CO_2 saturation profile on the seismic reflections originated from an incident 50-Hz Ricker wavelet, a typical band-limited seismic source.

The seismic traces in Figure 9 clearly show, as time increases, that the first reflection from the caprock/reservoir contact increases in amplitude as the contrast in the seismic velocities becomes larger due to the injection of CO_2 in the sandstone. The same occurs for the contact between the base of the sandstone layer and the top of the shale barrier. The amplitude increase in the response of the first contact becomes stationary once the effect of the CO_2 saturation in the velocities becomes rather negligible. As time passes (compare Figure 9 at $t = 1900$ and $t = 800$ days), the response associated with the sandstone/shale barrier contact shows a time

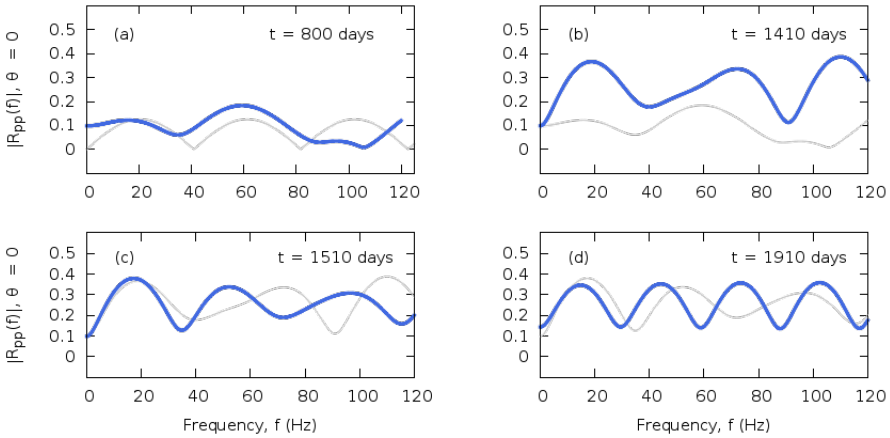

Figure 8: Normal-incidence frequency-dependent $|R_{\mathrm{pp}}(f)|$ reflectivity modulus for the reservoir with a CO_2 vertical distribution considering from the caprock to the base of the topmost shale barrier at $h = 160$ m. At *(a)* (t=800 days) there is no CO_2 saturation transition. *(b)* the transition starts to form (t=1410 days) and *(c)* the transition develops (t=1510 days). In *(d)* the transition has practically become a constant CO_2 saturation layer. The pre-injection sinusoidal character has been recovered and is rather stable now. Curves in gray show the previous state, in (a) being the pre-injection case

shift that individualizes its response from the one associated to the caprock/sandstone contact, which is clearly visible at $t = 1910$ days. This time shift is also related to the decay in velocity in the sandstone due to the CO_2.

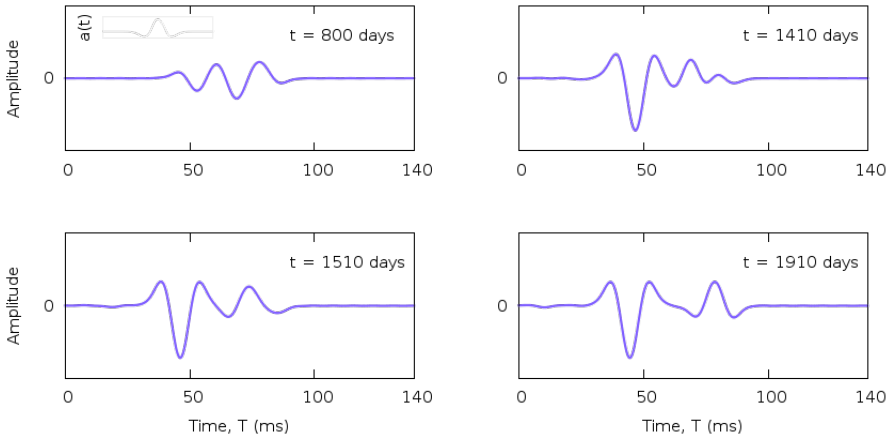

Figure 9: Synthetic traces from the resulting reflectivity of Figure 8 and 32 ms Ricker wavelet shown in the top left plot.

For comparison, and following Liner and Bodmann (2010), we also show the time-frequency response of the convolution of the reflectivity with a time-domain unit spike. The resulting time–frequency response is easier to interpret. For example, the amplitude ringing that marks that the CO_2 transition has give way to a constant saturation layer is more evident in Figure 10 than in 11. Obviously, frequency patterns beyond the central frequency of the source wavelet will be strongly attenuated, making the pattern interpretation more difficult to achieve in a real situation. By comparing Figures 10 and 11, we can inspect which features of the reflectivity will remain visible in the spectrogram associated with a seismic trace. Mainly the interpretation of the position of the amplitude notches that fall near the wavelet central frequency should aid to

the characterization of the vertical CO_2 distribution. As another tool that may help to interpret

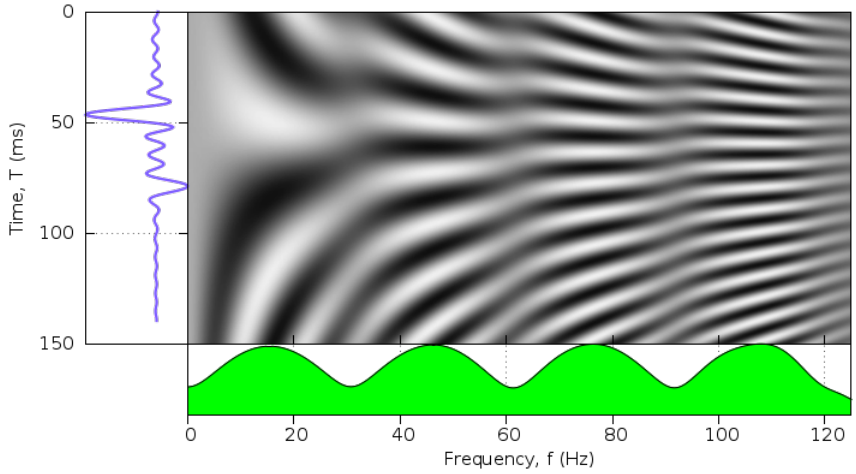

Figure 10: Waveform decomposition for the convolution of the reflectivity with a unit spike in time. $t = 1910$ days. the transition has turned into a constant CO_2 layer. The amplitude ringing in frequency in clearly evident.

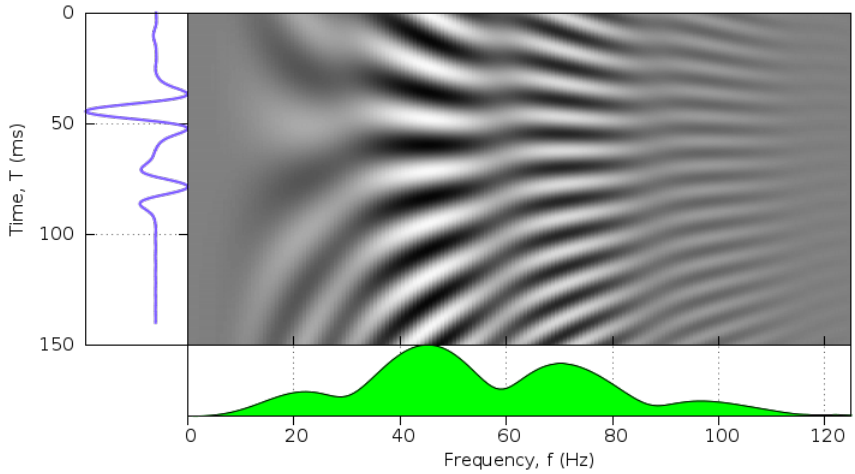

Figure 11: Waveform decomposition for the synthetic trace when $t = 1910$ days. The transition zone has turn into a constant CO_2 layer.

the evolution of the CO_2 accumulation, we analyze now the STFT response of the topmost part of the reservoir.

As the sandstone layer is not thick enough, the CO_2/brine contact can not be resolved in time. To inspect the frequency response, we computed the STFT for the convolution of the reflectivity with a time unit spike. The resulting time-frequency decomposition will have better time resolution than the ones computed directly from the synthetic traces because no effects due to the Ricker wavelet are introduced. A Hamming window of 12 ms was used when computing these spectrograms. Similar results, without the imprint of the wavelet can be generated by spectral balancing of the synthetic data.

The time-frequency amplitude of the STFT as seen in Figures 12 to 13, clearly shows the increase in resolution of the reservoir geological contacts as the time of the CO_2 injection in-

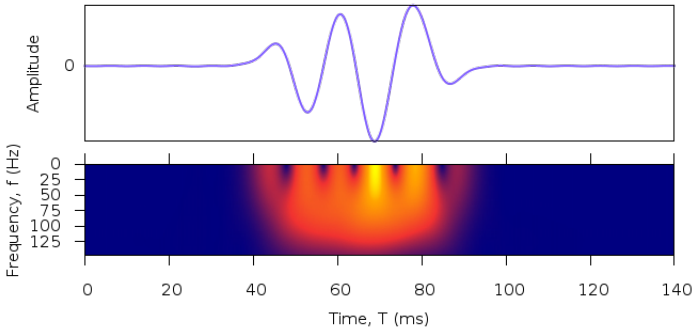

Figure 12: Amplitude spectra of the short time Fourier transform (STFT) of the synthetic trace when $t = 800$ days. The filter window is 95 ms long.

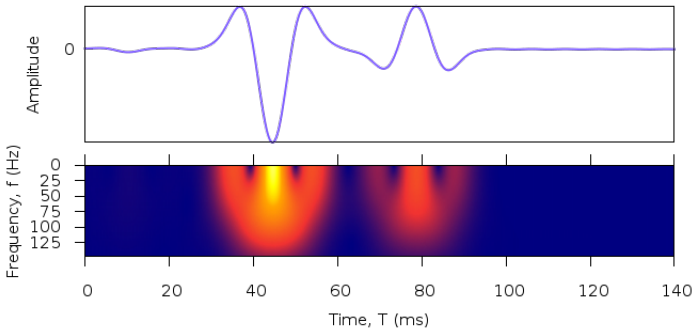

Figure 13: Amplitude spectra of the short time Fourier transform (STFT) of the synthetic trace when $t = 1910$ days. The filter window is 95 ms long.

creases. The highest amplitudes correspond to the caprock/sandstone contact reflection. No evidence on the fluid CO_2/brine contact is visualized. Higher resolution decomposition algorithms, such as matching pursuit (Chakraborty and Okaya, 1995) or a Wigner–Ville distribution (Xiaoyang and Tianyou, 2009) may exhibit better results in this reservoir scenario, since they bypass the intrinsic time-frequency resolution of the STFT (Castagna and Sun, 2006).

7 CONCLUSIONS

In this work we applied a finite difference relaxation scheme for the solution of the Buckley-Leverett equation for immiscible fluid flow and a coupled matrix propagator method for reflectivity and synthetic seismogram modeling. The method was applied to the study of the injection and vertical migration of CO_2 in a brine saturated sandstone. This allowed us to simulate the formation of the topmost CO_2 accumulation below the main caprock as well as temporal saturation transition zones below intra-reservoir permeability barriers. Time-frequency mapping and waveform simulations were also performed to improve the interpretation of the numerical results.

We analyzed the effect of capillary forces in the solution of the Buckley-Leverett equation,

showing that their influence on the location of the CO_2 saturation front are not important for monitoring purposes.

We have shown that the reflectivity character of a transition layer differs substantially from a constant CO_2 saturation layer. Although the presence of a CO_2 transition can be retrieved from the reflectivity, more information seems harder to obtain if the thickness of the target layer is not large enough. For favorable scenarios, temporal delineation of the CO_2 accumulation can be pursued from the time-frequency response.

The effects of the reflectivity associated to the CO_2 saturation profile on the amplitude spectrum of an incident Ricker wavelet was also analyzed. We found that the location of the amplitude notches near the central frequency of the wavelet may be useful for the characterization of the vertical CO_2 distribution.

As a conclusion we can state that the combined methodology presented may be used to efficiently simulate and track the fluid movement of a CO_2 plume in a stratified reservoir using seismic data. Future work includes the implementation of higher resolution spectral decomposition algorithms to investigate whether the presented methodology can be applied to real seismic data.

8 ACKNOWLEDGMENTS

This work was partially supported by CONICET (Argentina) PIP 112-200801-00952 and Programa de Incentivos, Universidad Nacional de La Plata (UNLP).

REFERENCES

Audigane P., Gaus I., Czernichowski-Lauriol I., Pruess K., and Xu T. Two-dimensional reactive transport modelling of CO_2 injection in a saline aquifer at the sleipner site, north sea. *American Journal of Science*, 307:974–1008, 2007.

Brekhovskik L.M. *Waves in layered media*. Academic, 1980.

Brooks R.H. and Corey A.T. Properties of porous media affecting fluid flow. *Journal of the Irrigation and Drainage Divison of the American Society of Civil Engineers*, 92(IR2):61–88, 1966.

Buckley S.E. and Leverett M.C. Mechanics of fluid displacement in sands. *Transactions of the American Institute of Minerals and Metallogenesis Engineering*, 146:107–116, 1942.

Carcione J.M., Picotti S., Gei D., and Rossi G. Physics and seismic modeling for monitoring CO_2 storage. *Pure and Applied Geophysics*, 163:175–207, 2006.

Castagna J.P. and Sun S. Comparison of spectral decomposition methods. *First Break*, 24:75–79, 2006.

Castagna J. P. S.S. and Siegfried R.W. Instantaneous spectral analysis: Detection of low-frequency shadows associated with hydrocarbons. *The Leading Edge*, 22(2):120–127, 2003.

Chadwick R.A., Arts R., and Eiken O. 4d seismic quantification of a growing CO_2 plume at sleipner, north sea. *Petroleum Geology: North-West Europe and Global Perspectives-Proceedings of the 6th Petroleum Geology Conference*, pages 1385–1399, 2005.

Chadwick R.A., Noy D., Lindeberg E., and Holloway S. Flow processes and pressure evolution in aquifers during the injection of supercritical CO_2 as a greenhouse gas mitigation measure. *Petroleum Geoscience*, 15:59–73, 2009.

Chadwick R.A., Zweigel P., Gregersen U., Kirby G.A., Holloway S., and Johannessen P.N. Geological reservoir characterization of a CO_2 storage site: The utsira sand, sleipner, northern north sea. *Energy*, 29:1371–1381, 2004.

Chakraborty A. and Okaya D. Frequency-time decomposition of seismic data using wavelet-based methods. *Geophysics*, 60(6):1906–1916, 1995.

Cunha M.C.C., Santos M.M., and Bonet J.E. Buckley-leverett mathematical and numerical models describing vertical equilibrium process in porous media. *International Journal of English Science*, 42(11-12):1289–1303, 2004.

Dubey R.K. A composite semi-conservative scheme for hyperbolic conservation laws. *amc*, 215:3335–3342, 2010.

Gomez J.L. and Ravazzoli C.L. Reflection characteristics of linear carbon dioxide transition layers. *Geophysics*, 77(3):D75–D83, 2012.

Goumiri I.R., Prévost J.H., and Preisig M. The effect of capillary pressure on the saturation equation of two-phase flow in porous media. *International Journal for Numerical and Analytical Methods in Geomechanics*, 2011.

Hayek M., Mouche E., and Mügler C. Modeling vertical stratification of CO_2 injected into a deep layered aquifer. 32:450–462, 2009.

Herty M., Seaïd M., and Singh A. A domain decomposition method for conservation laws with discontinuous flux function. *Applied Numerical Mathematics*, 57:361–373, 2007.

Jin S. and Z. X. The relaxation schemes for systems of conservation laws in arbitrary space dimensions. *Communications on Pure and Applied Mathematics*, 48:235–277, 1995.

Kaasschieter E.F. Solving the Buckley-Leverett equation with gravity in a heterogeneous porous medium. *Computational Geosciences*, 3:23–48, 1999.

Katahara K.W. Clay mineral elastic properties. *SEG Expanded abstracts*, 15(1):1691–1694, 1996.

Leverett M.C. Capillary behaviour in porous solids. *Transactions of the AIME Petrology and Engineering Division*, 142:152–169, 1941.

Liner C.L. and Bodmann B.G. The Wolf ramp: Reflection characteristics of a transition layer. *Geophysics*, 75(5):A31–A35, 2010.

Mavko G. and Mukerji T. Bounds on low-frequency seismic velocities in partially saturated rocks. *Geophysics*, 63(3):918–924, 1998.

Mavko G., Mukerji T., and Dvorkin J. *The Rock Physics Handbook: Tools for Seismic Analysis of Porous Media*. Cambridge University Press, 2nd. edition, 2011.

Mouche E., Hayek M., and Mügler C. Upscaling of CO_2 vertical migration through a period layered porous medium: The capillary-free and capillary-dominant cases. *Advances in Water Resources*, 33:1164–1175, 2010.

Negara A., El-Amin M.F., and S. S. Simulation of CO_2 plume in porous media: consideration of capillary and buoyancy effects. *International Journal of Numerical Analysis and Modeling, Series B*, 2(4):315–337, 2011.

Seaïd M. Stable numerical methods for conservation laws with discontinuous flux function. *Applied Mathematics and Computation*, 175:383–400, 2006.

Smith T.D., Sondergeld C.H., and Rai C. Gassmann fluid substitutions: A tutorial. *Geophysics*, 68:430–440, 2003.

Sweby P.K. High resolution schemes using flux limiters for hyperbolic conservation laws. *SIAM Journal of Numerical Analysis*, 21(5):995–1011, 1984.

Tsvankin I. *Seismic wavefields in layered isotropic media*. Samizdat Press, 1995.

Xiaoyang W. and Tianyou L. Spectral decomposition of seismic data with reassigned smoothed pseudo Wigner–Ville distribution. *Journal of Applied Geophysics*, 68:386–393, 2009.

Zhang C. and Ulrych T.U. Estimation of quality factors from CMP records. *Geophysics*, 67(5):1542–1547, 2002.